International Journal on Magnetic Particle Imaging
Vol 9, No 1, Suppl 1, Article ID 2303076, 4 Pages

Infinite Science Publishing

Proceedings Article

A system function component model for magnetic particle imaging with anisotropic particles

Marco Maass [a,*] · Christine Droigk [a] · Mathias Eulers [a] · Alfred Mertins [a,b]

[a] Institute for Signal Processing, University of Lübeck, Lübeck, Germany
[b] German Research Center for Artificial Intelligence (DFKI), AI in Biomedical Signal Processing, Lübeck, Germany
[*] Corresponding author, email: marco.maass@uni-luebeck.de

Abstract

In this work, it is demonstrated how an extended equilibrium magnetization model that allows modeling of uniaxial anisotropy for the nanoparticles can be integrated into the system function component model for magnetic particle imaging with a field-free point moving along a Lissajous trajectory. In previous works, the particle model with anisotropy has been shown to describe the measured system function better than the classical Langevin model of paramagnetism. However, the question arises how this model relates to the observed tensor products of the Chebyshev polynomials in the Fourier series components of the system function. Static uniaxial anisotropy is assumed in this work. It is shown that the structure compared to the isotropic solution can be preserved in this case.

I. Introduction

Magnetic particle imaging (MPI) measures the spatial distribution of superparamagnetic iron oxide nanoparticles (SPIOs) in a field of view (FOV). Since SPIOs have a nonlinear magnetization characteristic, spatio-temporally varying magnetic fields can be used to simultaneously measure the spatio-temporal distribution and concentration of SPIOs. For this purpose, different magnetic fields are applied to create a so-called field-free point (FFP) and move it along a trajectory. As a starting point for a mathematical model of the system function, the highly simplified Langevin model of paramagnetism was used [1]. This model is used in both Cartesian-like trajectory based MPI [2] and the Lissajous FFP-trajectory based MPI [3]. However, for multidimensional Lissajous FFP-trajectory based MPI this model is still too simple for good model based image reconstructions. In higher-dimensional MPI based on Lissajous FFP-trajectories, a relationship to tensor products of weighted Chebyshev polynomials (CPs) has been found in the Fourier series components of the system function, called system function components [3, 4]. Unfortunately, the model in [4] uses the oversimplified Langevin theory of paramagnetism. In contrast, more sophisticated Néel relaxation models have recently been proposed on basis of Fokker-Planck equations, one of these magnetization models shows higher similarity to measured system functions than the classical Langevin model [5]. From the Fokker-Planck equations (FPE), the equilibrium model (EQM) was derived in a next step [6, 7]. The advanced equilibrium model introduces a particle anisotropy but neglects the relaxation effects themselves. Nevertheless, the model seems to be promising for model based MPI. In this work it will be shown that the new equilibrium model from [6, 7] can be easily incorporated into the CP-based model in [4] if the additional assumption is made that the uniaxial easy axis is static in time.

10.18416/ijmpi.2023.2303076

II. Methods and materials

The voltage signal $u_\ell^{\mathrm{P}} : \mathbb{R} \to \mathbb{R}$ induced by particle distribution $c : \mathbb{R}^3 \to \mathbb{R}_+$ in the ℓ-th receive coil is commonly described mathematically by

$$u_\ell^{\mathrm{P}}(t) = -\mu_0 \frac{\mathrm{d}}{\mathrm{d}t} \int_{\mathbb{R}^3} c(\boldsymbol{x}) \boldsymbol{p}_\ell^{\mathrm{T}} \bar{\boldsymbol{m}}(\boldsymbol{x}, t) \, \mathrm{d}\boldsymbol{x}, \tag{1}$$

where $\bar{\boldsymbol{m}} : \mathbb{R}^3 \times \mathbb{R} \to \mathbb{R}^3$ denotes the mean magnetic moment vector (MMMV) of the SPIOs, $\boldsymbol{p}_\ell \in \mathbb{R}^3$ is a constant coil sensitivity, and μ_0 is the vacuum permeability.

The MMMV in the Langevin model is modeled by

$$\bar{\boldsymbol{m}}(\boldsymbol{x}, t) = m_0 \mathscr{L}(\beta \boldsymbol{H}(\boldsymbol{x}, t)), \tag{2}$$

where $\mathscr{L} : \mathbb{R}^3 \to \mathbb{R}^3$ is the three-dimensional Langevin function with $\mathscr{L}(\xi) = \mathscr{L}(\|\xi\|_2) \frac{\xi}{\|\xi\|_2}$, $\mathscr{L}(\xi) = \coth(\xi) - \frac{1}{\xi}$, $\boldsymbol{H} : \mathbb{R}^3 \times \mathbb{R} \to \mathbb{R}^3$ is the applied magnetic field, which is a superposition of the so-called periodic drive field (DF) $\boldsymbol{H}^{\mathrm{D}}(t)$ and the static selection field $\boldsymbol{H}^{\mathrm{S}}(\boldsymbol{x})$ with $\boldsymbol{H}(\boldsymbol{x}, t) = \boldsymbol{H}^{\mathrm{S}}(\boldsymbol{x}) + \boldsymbol{H}^{\mathrm{D}}(t)$, and $m_0, \beta \in \mathbb{R}$ are parameters.

In the equilibrium model with an uniaxial anisotropy the MMMV is described by [6, 7]

$$\begin{aligned} \bar{\boldsymbol{m}}(\boldsymbol{x}, t) &= m_0 \underbrace{\int_{\mathbb{S}^2} \boldsymbol{m} p_{\mathrm{N}}(\boldsymbol{m}, \beta \boldsymbol{H}, \alpha_{\mathrm{K_{anis}}}, \boldsymbol{n}) \, \mathrm{d}\boldsymbol{m}}_{= \mathscr{E}(\beta \boldsymbol{H}, \alpha_{\mathrm{K_{anis}}}, \boldsymbol{n})} \\ &= m_0 \mathscr{E}(\beta \boldsymbol{H}, \alpha_{\mathrm{K_{anis}}}, \boldsymbol{n}), \end{aligned} \tag{3}$$

where $p_{\mathrm{N}}(\boldsymbol{m}, \beta \boldsymbol{H}, \alpha_{\mathrm{K_{anis}}}, \boldsymbol{n}) = \frac{1}{\mathscr{Z}} \mathrm{e}^{\beta \boldsymbol{H}^{\mathrm{T}} \boldsymbol{m} + \alpha_{\mathrm{K_{anis}}} (\boldsymbol{n}^{\mathrm{T}} \boldsymbol{m})^2}$ is the probability density function (PDF) with respect to $\boldsymbol{m} \in \mathbb{S}^2$, $\mathbb{S}^2$ denotes the surface of the unit sphere, $\boldsymbol{n} : \mathbb{R}^3 \to \mathbb{S}^2$ denotes the easy axis of the particle anisotropy, $\alpha_{\mathrm{K_{anis}}} : \mathbb{R}^3 \to \mathbb{R}$ denotes the strength of the anisotropy, and $\mathscr{Z}(\beta \boldsymbol{H}, \alpha_{\mathrm{K_{anis}}}, \boldsymbol{n})$ normalizes $p_{\mathrm{N}}(\boldsymbol{m}, \beta \boldsymbol{H}, \alpha_{\mathrm{K_{anis}}})$ such that it is a PDF with respect to $\boldsymbol{m}$. It is assumed that $\boldsymbol{n}(\boldsymbol{x})$ and $\alpha_{\mathrm{K_{anis}}}(\boldsymbol{x})$ are static in time, besides, for $\alpha_{\mathrm{K_{anis}}}(\boldsymbol{x}) = 0$ it holds that (3) is equivalent to (2).

The system function of MPI $s_\ell(\boldsymbol{x}, t)$ is given by all terms in (1) that are independent of $c(\boldsymbol{x})$:

$$s_\ell(\boldsymbol{x}, t) = -\mu_0 \boldsymbol{p}_\ell^{\mathrm{T}} \frac{\partial \bar{\boldsymbol{m}}(\boldsymbol{x}, t)}{\partial t}. \tag{4}$$

For the Langevin model with a linear gradient field ($\boldsymbol{H}^{\mathrm{S}}(\boldsymbol{x}) = \boldsymbol{G}\boldsymbol{x}$, $\boldsymbol{G} \in \mathbb{R}^{3\times 3}$), the system function is expressed by

$$s_\ell(\boldsymbol{x}, t) = \boldsymbol{M}_\ell^{\mathrm{T}} \frac{\partial}{\partial t} \left[\mathscr{L}\left(\beta \boldsymbol{G} (\boldsymbol{x}_{\mathrm{FFP}}(t) - \boldsymbol{x}) \right) \right] \tag{5}$$

with the position of the FFP $\boldsymbol{x}_{\mathrm{FFP}}(t) = -\boldsymbol{G}^{-1} \boldsymbol{H}^{\mathrm{D}}(t)$ and $\boldsymbol{M}_\ell = \mu_0 m_0 \boldsymbol{p}_\ell$.

Without loss of generality, we restrict ourselves here to the 2D excitation case, for which it was shown in [4] that the system function components, i.e., the Fourier series coefficients of (5), can be represented by

$$s_{k\ell}(\boldsymbol{x}) = \mathrm{i}\omega_k \boldsymbol{M}_\ell^{\mathrm{T}} \int_{\mathbb{R}^3} \left[\tfrac{\partial^2}{\partial z_1 \partial z_2} \mathscr{L}\left(\beta \boldsymbol{G} \boldsymbol{z} \right) \right]_{\boldsymbol{z} = \boldsymbol{x} - \boldsymbol{y}} b_k(\boldsymbol{y}) \, \mathrm{d}\boldsymbol{y}, \tag{6}$$

Table 1: The physical parameters in the simulated models.

	symbol	value	unit
Magnetic constant	μ_0	$4\pi \times 10^{-7}$	$\mathrm{H\,m^{-1}}$
Boltzmann constant	k_B	$1.38064852 \times 10^{-23}$	$\mathrm{J\,K^{-1}}$
Particle diameter	D	25×10^{-9}	m
Particle volume	V_C	$\frac{\pi}{6} D^3$	$\mathrm{m^3}$
Particle temperature	T_B	300	K
Sat. magnetization	M_S	474000	$\mathrm{J\,m^{-3}\,T^{-1}}$
Magnetic anisotropy gradient	$g_{\mathrm{K_{anis}}}$	1250	$\mathrm{J\,m^{-3}}$
	m_0	$V_C M_S$	$\mathrm{J\,T^{-1}}$
	β	$\frac{\mu_0 V_C M_S}{k_B T_B}$	$\mathrm{mA^{-1}}$

where $k \in \mathbb{Z}$, $b_k(\boldsymbol{x})$ is related to a series of tensor products of CPs of second kind, $\omega_k = \frac{2\pi k}{T_{\mathrm{D}}}$, and T_{D} is the period length of $\boldsymbol{x}_{\mathrm{FFP}}(t)$.

For the MMMV in (3), the corresponding form of (5) is

$$s_\ell(\boldsymbol{x}, t) = \boldsymbol{M}_\ell^{\mathrm{T}} \frac{\partial}{\partial t} \left[\mathscr{E}\left(\beta \boldsymbol{G} (\boldsymbol{x}_{\mathrm{FFP}}(t) - \boldsymbol{x}), \alpha_{\mathrm{K_{anis}}}(\boldsymbol{x}), \boldsymbol{n}(\boldsymbol{x}) \right) \right]. \tag{7}$$

Both (5) and (7) are similar in their mathematical structure, therefore the solution for the system function components will be

$$\begin{aligned} s_{k\ell}(\boldsymbol{x}) = \mathrm{i}\omega_k \boldsymbol{M}_\ell^{\mathrm{T}} \int_{\mathbb{R}^3} \left[\tfrac{\partial^2}{\partial z_1 \partial z_2} \mathscr{E}\left(\beta \boldsymbol{G} \boldsymbol{z}, \alpha_{\mathrm{K_{anis}}}(\boldsymbol{x}), \boldsymbol{n}(\boldsymbol{x}) \right) \right]_{\boldsymbol{z} = \boldsymbol{x} - \boldsymbol{y}} \\ \cdot b_k(\boldsymbol{y}) \, \mathrm{d}\boldsymbol{y}. \end{aligned} \tag{8}$$

Note that this convolution integral represents a spatial convolution with a spatially varying kernel.

III. Experiments

In the numerical simulation, the proposed model B3 in [5] is used, where the easy axis $\boldsymbol{n}(\boldsymbol{x}) = \frac{\boldsymbol{H}^{\mathrm{S}}(\boldsymbol{x})}{\|\boldsymbol{H}^{\mathrm{S}}(\boldsymbol{x})\|_2}$ is aligned at the selection field and the anisotropy strength is spatially varying with $\alpha_{\mathrm{K_{anis}}}(\boldsymbol{x}) = \frac{g_{\mathrm{K_{anis}}} V_C}{k_B T_B} \frac{\|\boldsymbol{H}^{\mathrm{S}}(\boldsymbol{x})\|_2}{\max_{\boldsymbol{x} \in \Omega} \|\boldsymbol{H}^{\mathrm{S}}(\boldsymbol{x})\|_2}$.

For the experiments, the system function is numerically simulated by discretizing (7) in the variables t and $\boldsymbol{x}$, and then the system function components are approximated using the discrete Fourier transform (DFT). This is used as the ground-truth system function component $s_{\ell k}^g(\boldsymbol{x}_n)$, where $\boldsymbol{x}_n$ with $n = 1, 2, \ldots, N_{\mathrm{pixel}}$ denotes the spatially uniform sampling position. For the system function component model (8), we discretized the convolution integral and perform the discrete convolution, resulting in $s_{\ell k}^a(\boldsymbol{x}_n)$. The SPIOs parameter are listed in the Table 1. For the scanner simulation, a two-dimensional FFP trajectory was simulated with the frequency ratio $f_x / f_y = 17/16$ and a repetition time $T_{\mathrm{D}} = 652.8\,\mu\mathrm{s}$, covering a DF-FOV range of 24 mm × 24 mm. The system function was sampled on an overscan region of size 65 mm × 65 mm discretized to 121 × 121 pixels. One period of the FFP is sampled at 16000 sample points in time. The formal series $b_k(\boldsymbol{y})$ is truncated after [4] to 121 terms. Each weighted CP is sampled with an oversampling factor of 16, followed by a lowpass filtering and

10.18416/ijmpi.2023.2303076

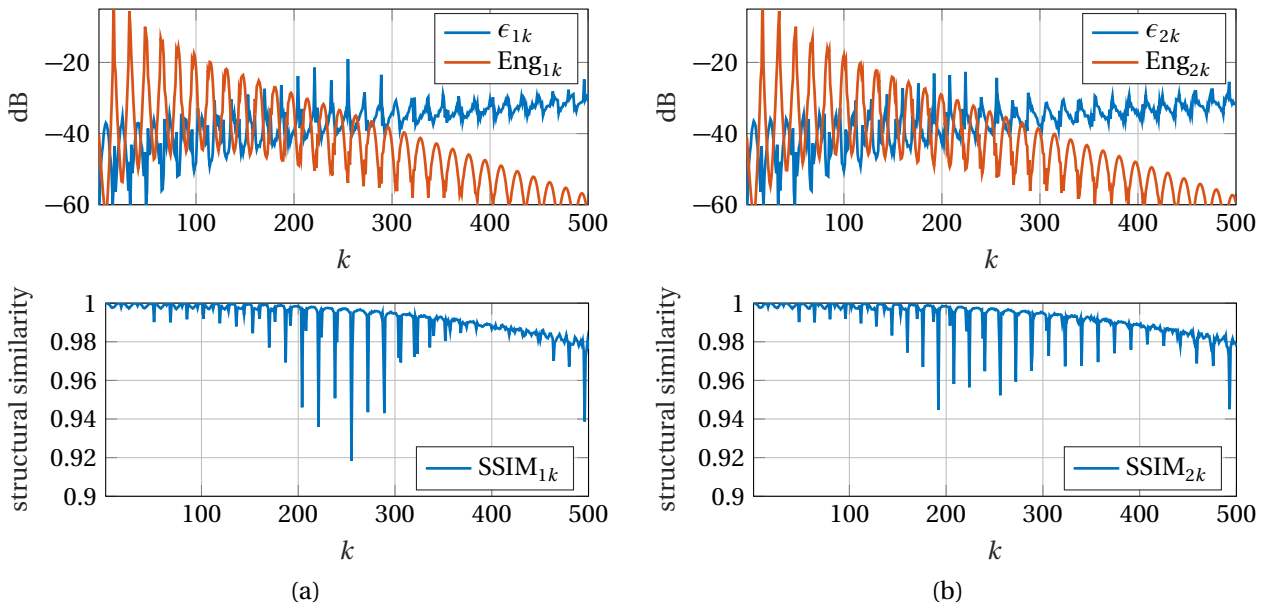

Figure 1: Upper Row: The relative numerical error $\epsilon_{\ell k}$ and the energy of the ground-truth system function component $\mathrm{Eng}_{\ell k}$. Lower Row: The SSIM between the ground-truth system function component and the system function component by (8). (a) Result with respect to the first component. (b) Result with respect to the second component.

downsampling with a factor of 16 to avoid spatial aliasing, then the lowpass filtered CPs are convolved with the magnetization model. Afterwards, the FOV is again reduced to the DF-FOV to avoid boundary artifacts due to the spatially limited convolution. The similarity of both system function components is compared by the relative numerical error,

$$\epsilon_{\ell k} = \frac{1}{N_{\text{pixel}}} \sum_{n=1}^{N_{\text{pixel}}} \left| \frac{s^g_{\ell k}(\boldsymbol{x}_n)}{\max_m(|s^g_{\ell k}(\boldsymbol{x}_m)|)} - \frac{s^a_{\ell k}(\boldsymbol{x}_n)}{\max_m(|s^a_{\ell k}(\boldsymbol{x}_m)|)} \right|^2,$$

the normalized energy for the ground-truth system function components,

$$\mathrm{Eng}_{\ell k} = \frac{\sum_{n=1}^{N_{\text{pixel}}} |s^g_{\ell k}(\boldsymbol{x}_n)|^2}{\max_{m\in\mathbb{Z}}\left(\sum_{n=1}^{N_{\text{pixel}}} |s^g_{\ell m}(\boldsymbol{x}_n)|^2\right)},$$

and the structural similarity index measure (SSIM) [8] using the Matlab built-in function by

$$\mathrm{SSIM}_{\ell k} = \mathrm{ssim}\left(\left|s^a_{\ell k}(\boldsymbol{x}_n)\right|, \left|s^g_{\ell k}(\boldsymbol{x}_n)\right|\right).$$

IV. Results and discussion

In Fig. 1 (upper row) it can be seen that the relative numerical error $\epsilon_{\ell k}$ between the ground-truth system function components and the function calculated with (8) is always smaller than 20dB in the first 500 frequency components. In addition, one can see that the relative numerical error is high when the normalized energy is quite low and vice versa. In tendency, the normalized energy of the $s^g_{\ell k}(\boldsymbol{x}_n)$ decreases with increasing values for k. Additionally, oscillatory behavior is observed, where values k with locally large energy correspond to a low mixing order ($|m_x|, |m_y|$) and vice versa [3]. The mixing orders correspond to the lowest order tensor product of CPs and are related to the spatial structure of the system function components [3, 4]. In the lower row of Fig. 1, one can observe that the SSIM is always larger than 0.92 for all k. This indicates that the structural patterns between $|s^g_{\ell k}(\boldsymbol{x}_n)|$ and $|s^a_{\ell k}(\boldsymbol{x}_n)|$ are highly correlated. For larger values of k, a slightly decreasing SSIM can be detected. For pure multiples of the frequency dividers a slight systematic degradation of the SSIM can be observed. In such cases, the mixing factor of one of the coefficients $|m_x|$ or $|m_y|$ is zero and therefore the convolution is no longer performed with a spatially bounded CP of second kind [4, Theorem 6.1.], leading to a truncation error. The low-energy frequency components correspond to weighted high-order CPs, but they oscillate strongly, therefore, for a fixed spatial discretization of the convolution integral in (8), the relative numerical error is expected to increase. However, in real-world systems the structural patterns of the low-energy frequency components have usually disappeared in the noisy scanner background. Both receive paths (see Figs. 1 (a) and (b)) show the same behavior. In Fig. 1., the relative numerical error is small and SSIM is high for both receiving paths in the tested scenario, indicating that both models are approximately equivalent in (7) and (8).

The model used in this work, i.e. (3) with model B3 from [5], has its motivation in the observation that the model better describes the spatial structure of a system matrix than the model based on the classical Langevin

function, even though it is pointed out in [5] that the model is an approximate model rather than a physical model. In the work [7] the situation was systematically studied in which the FPE model and EQM are approximately equivalent. Considering the parameters in Table 1 and comparing them with the results in [7, Table 1], the EQM should match well with the model in [5, B3]. Concerning the assumption of a time-invariant easy axis $\boldsymbol{n}(\boldsymbol{x})$ and an anisotropy strength $\alpha_{\mathrm{K}_{\mathrm{anis}}}(\boldsymbol{x})$ in (8), the time-invariant model could be justified under certain circumstances. Exemplary, there are medical scenarios conceivable in which medical instruments could be coated with immobilized particles that can additionally have a fixed, oriented easy axis. Such approach would be useful to determine the orientation and position of medical instruments such as catheters, stens, etc. during an MPI measurement [9, 10].

In the extended EQM, the actual relaxation is not included, but simple relaxation models could be included. Relaxation effects, which are caused by spatio-temporal effects, however, are not to be considered without further steps in (8). All models in this work are based on a time-invariant SPIO distribution $c(\boldsymbol{x})$, but SPIOs are ferrofluids that can be spatially deformed by time-varying magnetic fields, so in practice $c(\boldsymbol{x}, t)$ holds to some extent. Fortunately, one would expect the influence to be periodic in the mean as well, as long as the SPIO distribution is not completely free to move in the medium and one has reached a steady-state in the MPI measurement. However, if the SPIO distribution is subject to other diffusion processes, e.g. in blood flow, the model (8) is inaccurate and a reconstruction algorithm would lead to motion artifacts. How to deal with such inaccuracies is investigated in [11]. It should be mentioned that the simulation of (8) is computationally much more demanding than the simulation via (7) followed by a DFT. The advantage of the expression (8) over (7) is that it directly represents the spatial structure of the system function components, which might be helpful in a parameter identification task or when trying to find good models for $\boldsymbol{n}(\boldsymbol{x})$ and $\alpha_{\mathrm{K}_{\mathrm{anis}}}(\boldsymbol{x})$.

V. Conclusion

We have shown that it is possible to introduce into the mathematical model in [4] a more sophisticated magnetization model that allows spatially varying but temporal invariant SPIO anisotropies to be modeled. Exemplarily, it is demonstrated that the structural pattern is a result of the chosen FFP trajectory interacting with the magnetization model. Although these results seem to be of limited value, they show that CPs play a role in more complex models and probably contribute to a better mathematical understanding of MPI. Yet it also seems possible to combine spatially varying convolution with the direct reconstruction model in [12] for the deconvolution step.

Author's statement

Authors state no conflict of interest.

References

[1] J. Weizenecker, J. Borgert, and B. Gleich. A simulation study on the resolution and sensitivity of magnetic particle imaging. *Physics in Medicine and Biology*, 52(21):6363–6374, 2007, doi:10.1088/0031-9155/52/21/001.

[2] P. Goodwill, G. Scott, P. Stang, and S. Conolly. Narrowband magnetic particle imaging. *IEEE Transactions on Medical Imaging*, 28(8):1231–1237, 2009, doi:10.1109/TMI.2009.2013849.

[3] J. Rahmer, J. Weizenecker, B. Gleich, and J. Borgert. Signal encoding in magnetic particle imaging: Properties of the system function. *BMC Medical Imaging*, 9(4):4, 2009, doi:10.1186/1471-2342-9-4.

[4] M. Maass and A. Mertins. On the representation of magnetic particle imaging in Fourier space. *International Journal on Magnetic Particle Imaging*, 6(1), 2020, doi:10.18416/IJMPI.2019.1912001.

[5] T. Kluth, P. Szwargulski, and T. Knopp. Towards accurate modeling of the multidimensional magnetic particle imaging physics. *New Journal of Physics*, 21(10):103032, 2019, doi:10.1088/1367-2630/ab4938.

[6] M. Maass, C. Droigk, M. Eulers, and A. Mertins. An analytical equilibrium solution to the Néel relaxation Fokker-Planck equation. *International Journal on Magnetic Particle Imaging*, 8(1 Suppl. 1), 2022, doi:10.18416/IJMPI.2022.2203008.

[7] H. Albers and T. Kluth. Immobilized nanoparticles with uniaxial anisotropy in multi-dimensional Lissajous-type excitation: An equilibrium model approach. *International Journal on Magnetic Particle Imaging*, 8(1 Suppl. 1), 2022, doi:10.18416/IJMPI.2022.2203048.

[8] Z. Wang, A. Bovik, H. Sheikh, and E. Simoncelli. Image quality assessment: From error visibility to structural similarity. *IEEE Transactions on Image Processing*, 13(4):600–612, 2004, doi:10.1109/TIP.2003.819861.

[9] M. Möddel, F. Griese, T. Kluth, and T. Knopp. Estimating the spatial orientation of immobilized magnetic nanoparticles with parallel-aligned easy axes. *Phyical Review Applied*, 16:L041003, 4 2021, doi:10.1103/PhysRevApplied.16.L041003.

[10] H. Albers, T. Knopp, M. Möddel, M. Boberg, and T. Kluth. Modeling the magnetization dynamics for large ensembles of immobilized magnetic nanoparticles in multi-dimensional magnetic particle imaging. *Journal of Magnetism and Magnetic Materials*, 543:168534, 2022, doi:10.1016/j.jmmm.2021.168534.

[11] C. Brandt and C. Schmidt. Modeling magnetic particle imaging for dynamic tracer distributions. *Sensing and Imaging*, 22(45), 2021, doi:10.1007/s11220-021-00368-w.

[12] C. Droigk, M. Maass, and A. Mertins. Direct multi-dimensional Chebyshev polynomial based reconstruction for magnetic particle imaging. *Physics in Medicine and Biology*, 67(4):045014, 2022, doi:10.1088/1361-6560/ac4c2e.